Near-Field Asymmetries in Plasmonic Resonators

Vladimir Aksyuk,[a] Basudev Lahiri,[a,b] Glenn Holland,[a] and Andrea Centrone[a]*

a NIST, Center for Nanoscale Science and Technology, Gaithersburg, 100 Bureau Drive, MD 20899 (USA)
e-mail: andrea.centrone@nist.gov
b University of Maryland, Institute for Research in Electronics and Applied Physics (IREAP), College Park, MD 20742 (USA).

Surface-enhanced infrared absorption (SEIRA) spectroscopy exploits the locally enhanced field surrounding plasmonic metamaterials to increase the sensitivity of infrared spectroscopy. Light polarization and incident angle are important factors for exciting plasmonic nanostructures; however, such angle dependence is often ignored in SEIRA experiments, typically carried out with Cassegrain objectives. Here, the photothermal induced resonance technique and numerical simulations are used to map the distribution and intensity of SEIRA hot-spots surrounding gold asymmetric split ring resonators (ASRRs) as a function of light polarization and incidence angle. Results show asymmetric near-field SEIRA enhancements as a function of the incident illumination direction which, in analogy with the symmetry-breaking occurring in asymmetric transmission, we refer to as symmetry-breaking absorption. Numerical calculations reveal that the symmetry-breaking absorption in ASRRs originates in the angle-dependent interference between the electric and magnetic excitation channels of the resonators' dark-mode. Consequently, to maximize the SEIRA intensity, ASRRs should be illuminated from the dielectric side at an angle that maximizes the constructive interference of the two excitation channels (35° for the structures studied here), in place of the Cassegrain objectives. These results are can be generalized to all structures characterized by plasmonic excitations that give raise to a surface-normal magnetic moment and that possess an electric dipole.

Introduction

The collective oscillation of conduction electrons in plasmonic materials allows engineering both their resonant optical response from the visible to THz and to couple propagating light with nanoscale volumes of matter (hot-spots). These characteristic properties of plasmonic devices enable new applications in fields like therapeutics,[1, 2] energy,[3] and sensing.[4, 5] For example, such locally enhanced light-matter interactions are exploited by surface-enhanced Raman[5-9] and surface-enhanced infrared absorption[4, 9-14] (SEIRA) spectroscopies for sensitive chemical detection. A particularly interesting structure is the Asymmetric Split Ring Resonator (ASRR),[15-18] which is composed of two arcs of different length sharing a common center of curvature. ASRRs have plasmonic resonances that are tunable in the IR spectral range, as a function of the diameter of the resonator, and therefore they are promising for SEIRA applications.[10] It is well known that the light polarization[10, 15, 16, 18] and incident angle[19-22] strongly influence the plasmonic response of ASRRs and other plasmonic materials; however, such angle dependence is not usually considered in SEIRA experiments. For example, the Cassegrain objectives[10] commonly used in IR microscopes illuminate the sample and collect light with a rotationally symmetric angular range close to normal incidence.

In this work, the photothermal induced resonance (PTIR) technique[10, 23-28] and numerical analysis are used to study the near-field SEIRA enhancement in poly(methyl methacrylate) (PMMA) films coating gold ASRR structures illuminated through a dielectric substrate at ± 45° with respect to the plane of the resonators. PTIR,[10, 24, 25, 27, 29-31] is an emerging technique that, by combing the lateral resolution of Atomic Force Microscopy (AFM) and chemical specificity of IR spectroscopy, enables IR analysis at the nanoscale. PTIR images and spectra revealed different (i.e. symmetry-breaking) near-field SEIRA enhancements for illumination angles ± 45° with respect to the surface normal (i.e. the optical axis of the resonators). In analogy with symmetry-breaking "asymmetric transmission", we refer to this effect as symmetry-breaking absorption.

One ASRR plasmonic mode where the electric dipoles of the two arcs have opposite phase is referred to as the "dark mode"[32] because in a perfectly symmetric structure the arc dipoles would cancel each other and suppress the electric dipolar coupling with radiation and the related radiation loss. However, due to the circular displacement currents, this mode has a large magnetic dipole moment that radiates strongly at non-normal incidence angles. Therefore at non-normal incidence the ASRR's dark mode couples to incident light via dipolar interaction with both its electric moment (which is not completely suppressed by symmetry) and the

large magnetic moment. The numerical calculations reported below show that the experimentally observed symmetry-breaking absorption in these structures is caused by the angle-dependent interference between their dark mode's electric and magnetic excitation channels.

Based on these observations we suggest that for symmetric and slightly asymmetric SRRs the best excitation efficiency in SEIRA experiments occurs with *s*-polarized (TE) light incident from the dielectric side at angles far from surface normal and specifically for the angle which maximizes the constructive interference of the plasmonic excitation. This can be practically realized using a dielectric prism, as in this work, or with an attenuated total reflection (ATR) objective, in place of the most commonly used Cassegrain objectives. Furthermore, although the optical effects studied in this work are reciprocal, i.e. they do not violate the time-reversal property of the linear Maxwell's equations, we reason that the symmetry-breaking absorption observed here could be exploited to realize ultra-thin non-reciprocal reflectors and optical diodes by coating plasmonic resonators with a thin film of a nonlinear material.

Results

In this work gold ASRR arrays were fabricated directly on Zinc Selenide (ZnSe) optical prisms using a combination of Electron Beam Lithography and lift-off techniques (**Figure S1** of the supporting information).[10] The nanofabrication on these unusual substrates was made possible by custom adaptor pieces described previously.[24] The ASRRs samples studied here (**Figure S2**) have thickness of 150 nm ± 10 nm, an external diameter of 2.0 μm ± 0.1 μm, an internal diameter of 0.95 μm ± 0.10 μm as determined by AFM, unless otherwise noted. All uncertainties in the manuscript represent a single standard deviation.

Sample-1 (Figure S2a) is a square array consisting of gold resonators all with the same orientation and was used as a reference. *Sample-2* (figure S2b) and sample 3 (Figure S2c) were obtained by repeating a unit cell of 4 ASRRs each rotated in plane by 90°. These latter arrays enable studying the dependence of the SEIRA enhancement on the angle of incidence (± 45°) and on the direction of linearly polarized light in the sample plane with respect to the resonators' orientation in a single PTIR experiment. *Sample-3* is similar to *Sample-2* but it was fabricated with a unit cell rotated by 90° relative to the one of *Sample-2* and with a pitch between the resonators of 10.0 μm ± 0.1 μm (Figure S2c).

In this paper we denote with ϑ the light incident angle with respect to the normal of the sample plane. The sample is illuminated from the air side in FTIR experiments (**Figure 1**) and from the dielectric side in PTIR experiments (**Figure 2,3**) and in the numerical simulations (**Figure 4, 5**). The PTIR experiments were carried out at a fixed angle (45°). Since *Sample-2* and *Sample-3* have resonators with different orientations with respect to the incoming beam, to facilitate the comparison with the simulations it is convenient to refer to ϑ = +45° (with positive sign) for the illumination of a resonator from the short arc side and to ϑ = -45° (with negative sign) for the illumination of a resonator from the long arc side.

The plasmonic modes of metallic structures in close proximity couple via near-field interactions and their optical properties are well described by the plasmon hybridization model.[33, 34] The fundamental plasmonic modes of two similar structure arcs in close proximity hybridize, forming symmetric and antisymmetric normal modes (see figure 1d). The symmetric "bright" mode has a large net electric dipole because the two arcs have in-phase electric polarization vectors, which lead to strong interaction with incident light. The lower-energy antisymmetric "dark" mode,[32] has, instead, the arcs' electric polarization vectors in approximately opposite phase in the two arcs (figure 1d). Since both the bright- and dark-mode have similar energies, near normal incidence both can be excited simultaneously (e.g. **Figure S5b**, **Figure S6**). However, because the dark mode has a higher quality factor and a strong magnetic dipolar coupling, it is excited much more strongly than the bright mode when illuminated at 45° incidence from dielectric side as in PTIR experiments (Figure 5a,b, Figure S5a, Figure S6). Therefore the dark mode dominates the overall structure response and will be the main focus of our discussion.

The effect of linearly polarized light on the resonators' response was studied first by recording the far-field FTIR with a Cassegrain objective which illuminates the samples from the air side from all directions with a range of incidence angles from sample surface normal (15° < ϑ < 30°, Figure 1). The IR spectra of *sample-1* show that the excitation of the ASRRs' plasmonic resonances is strongly polarization dependent, as expected.[10, 15] In particular, for the electric field polarization parallel to the long direction of the arcs (hereafter parallel polarization, blue arrow in figure 1b), the reflectivity is higher than for bare ZnSe (used as reference) and presents a narrow Fano resonance on top of a broader background, which is attributed to the interference of the dark-mode with the bright mode and background reflection.[10, 15, 16, 18] The reflectivity for perpendicular polarization (red arrow in figure 2b) is much weaker and lacks spectral features. For perpendicular polarization the electric dipolar coupling with radiation is forbidden by symmetry and magnetic coupling for dark mode is very weak for angles close to the surface normal, air side. *Sample-2* shows the same response for both parallel and perpendicular polarization. In particular, it retains the Fano resonance stemming from the dark-mode, albeit with smaller modulation contrast on top of an overall reduced reflectivity compared to *sample-1*. This is consistent with a combination of broad scattering from structures unfavorably oriented with respect to the light polarization (identified by red arrows in Figure1c), and a weaker response due to fewer structures oriented parallel to the incident field, compared to *sample-1* (identified by blue arrow in Figure 1c). Additionally, we hypothesize that the different orientation of the resonators with respect to their first neighbors may results in a disruption of nearest-neighbor coupling and loss of the scattering enhancement via the coherent array effect[9, 11, 12] in *sample-2*.

Few optical and electronic microscopy techniques are capable to provide high resolution maps of the plasmonic excitation in nanomaterials and have been the subject of a recent review.[35] For example scattering scanning near-field optical microscopy (s-SNOM) has been extensively applied to map the electric-field surrounding plasmonic nanostructures.[4, 36-40] In general, however, s-SNOM requires a tip-specific modelling[41, 42] to accurately describe the tip-sample-substrate interactions in the near-field for extracting quantitative information. In fact, the s-SNOM signal is a function, of the sample complex refractive index (i.e. of sample absorption and scattering), but also of the tip-sample relative size,[43] thus resulting in spectral lineshapes that may not correlate with far-field IR spectra[44] and may show Fano-shaped resonances.[36] This effect is particular severe for samples with strong IR absorption peaks or in the case of SEIRA, where the high sensitivity is linked to strong absorption and is typically accompanied by Fano distortions[17], which can complicate chemical identification. To the best of our knowledge, no near-field spectra of SEIRA hot-spots have been recorded with s-SNOM.

PTIR,[10, 24, 25, 29, 30] also known as AFM-IR,[27, 31, 45] is an emerging technique that combines the lateral resolution of Atomic Force Microscopy (AFM) and chemical specificity of IR spectroscopy enabling chemical imaging well beyond the diffraction limit of IR light. PTIR was applied for nanoscale characterization of bacteria,[27, 31] polymers,[24-26] inorganic nanoparticles,[25, 46] organic nanocrystals,[29] metal-organic framework materials[47] and cells.[30, 48] Notably, the PTIR signal is proportional to the absorbed energy[24] (not scattering) and the PTIR spectra are directly comparable with IR spectral libraries,[26] allowing for materials identification and enabling the acquisition of near-field spectra that are free of Fano distortions for both SEIRA hot spots[10] and plasmonic excitations.[49] For example, recently we used the PTIR technique to map and quantify SEIRA near-field hot-spots in gold ASRR arrays (made with resonators all with the same orientation) as a function of light polarization and resonator size.[10]

PTIR samples are placed on an optically transparent prism and are illuminated at $\vartheta = 45°$ with a tunable IR pulsed laser through total internal reflection (**Figure 2a**). The absorption of a laser pulse by the sample induces heating, sample expansion, and mechanical excitation of the AFM cantilever that is in contact with the sample and is monitored by a four-quadrant detector. After moving the AFM tip to the location of interest, a local infrared spectrum is obtained by plotting the maximum amplitude of the tip deflection as a function of the optical frequency. PTIR maps are obtained by illuminating the sample at a constant frequency while scanning the AFM tip.[10, 24, 25, 31] The typical laser spot size at the sample is ≈ 30 μm, but the AFM tip functions as a "spatial filter" allowing the extraction of spectroscopic information with nanoscale spatial resolution, well beyond the diffraction limit of IR light.[10, 24, 26, 27] A polarization control module consisting, of three motorized mirrors, is used to obtain the desired light polarization at the sample.[10, 45]

After recording the FTIR spectra all resonators were coated with a 200 nm PMMA film, used to probe the near-field absorption enhancement in the PTIR experiments.[10] Figure 2b, c shows the AFM height and PTIR images recorded in correspondence of PMMA CH_3 wagging mode[50] absorption at 1191 cm^{-1} (8.40 μm) for *sample-2*. The ASRRs structures buried under the PMMA layers are barely visible in the height images (fig. 4a); nevertheless, the PTIR absorption images prominently show hot-spots in the near-field (fig. 4b). Since the PTIR signal intensity is proportional to the local absorbed energy,[24] the PTIR maps directly show the absorption enhancement in the near-field.[10]

In the PTIR experiments the laser light is incident on the ASRRs at 45° angle (figure 2a) and has the electric field vector in the resonators plane. Within a single PTIR image field, *sample-2* has resonators with four different orientations relative to the incident beam. The incident electric field is parallel to the arcs for half of the resonators and perpendicular to the other half (fig 2d inset). Naively, one could expect that only the resonators excited by light with parallel polarization will be efficiently excited. As expected, the resonators excited with perpendicular light polarization show very weak hot spots. However, the data reveals that the near-field hot-spot intensities for the resonators excited with parallel polarization (for example the two leftmost resonators in the highlighted box in figure 2b) are very different. While the light polarization is parallel for both the top-left and the bottom-left resonators in figure 2c, per our convention the resonators are effectively illuminated $\vartheta = +45°$ and $\vartheta = -45°$, respectively, because they are rotated by 180° with respect to each other.

To experimentally quantify the asymmetry, near-field PTIR spectra (Figure 4d) were taken from the hot-spots locations of the two resonators and compared to the PMMA spectra obtained away from the array (used as reference). Based on the spectra intensity, the near field maximum enhancement (at 1180 cm^{-1}) normalized to the PMMA reference is estimated to be 7.8 ± 0.2 and 2.6 ± 0.1 for the hot spots identified by the red and blue "+"in figure 4c, respectively. As we describe below, the near-field response of the resonators is dominated by the narrow dark-mode. The bright-mode instead does not concentrate the field in the hot-spot nearly as efficiently as the dark-mode but provides a fairly strong far-field scattering signal. Consequently, the spectral region with the largest SEIRA enhancement depends mostly on the spectral overlap between the PMMA absorption peaks and the dark-mode excitation. By analyzing closely spaced ASRRs any possible effect of beam inhomogeneity is minimized, however, the near field interactions between neighboring structures may not be negligible (see supplemental discussion 1 in the supporting information and figure S3).

The 10 μm pitch between resonators in *sample-3* minimizes the interaction between adjacent resonators and allows studying the SEIRA enhancement in single resonators, confirming (**Figure 3**) the observations on the denser *sample-2*. In addition to the hot-spots in proximity of the arc termination, the PTIR image in figure 3b shows enhanced absorption to the right of the two bottom resonators, revealing a standing wave interference pattern due to the interference of the incident light with the light scattered directionally by the resonators. While PTIR doesn't measure scattering directly, the scattered light is detected here indirectly (for the first time with this technique) by measuring the absorption in the dielectric film. The spatially oscillating pattern observed to the

right of the resonators in the experiment is also found in the results of the numerical simulations (see below, supplementary **Figure S4**).

To understand the physics behind the experimentally observed symmetry-breaking absorption, a frequency domain finite element method was used to calculate full vector time-harmonic electromagnetic fields in and around a single gold ASRR similar to *sample-3*. The resonator in the simulation was placed on a ZnSe surface, covered by a PMMA film and illuminated by a plane wave from inside ZnSe. Since PTIR can measure the SEIRA enhancement only if absorption in the dielectric is not negligible, the experiments were recorded at wavelengths corresponding to strong PMMA absorption peaks. However, numerically we have modeled the electromagnetic fields for a broader range of frequencies and incidence angles (**Figure 4a, b**). Specifically, in case of parallel polarization, the calculations were carried out for a range of incident angles ($-60° < \vartheta < 60°$, see Figure 4a) while for perpendicular polarization the calculation were carried out only for $\vartheta = 45°$ (figure 4b). Indices of refraction of 2.4 and 1.4 for ZnSe and PMMA, were used respectively and a wavelength-dependent, complex index of refraction was used for Au.[51] While in these calculations the absorption in the PMMA layer was neglected to focus on the plasmonic effects, numerical results can still be used to qualitatively model the PTIR experiments because the PTIR signal is proportional to the field energy density in the dielectric layer (obtained in the calculations) times the PMMA absorption coefficient.

Figure 4 shows that the model qualitatively reproduces the observed near-field SEIRA enhancement pattern of the PTIR experiments for $\vartheta = 45°$ for both parallel (Figure 4a) and perpendicular (Figure 4b) polarizations. The simulation show two strong hot-spots in the resonator's gaps for parallel polarization but only one hot-spot for perpendicular polarization (with two weaker spots outside the resonator, in accord with experiments). The supplementary discussion 2 of the SI provide an explanation for the hot spots distribution in the case of perpendicular polarization (which was observed before[10] but not explained). For the parallel polarization, the response can be understood as a superposition of bright and dark modes. The arcs form a loop, and the dark-mode's displacement currents flowing in a circle create an out-of-plane magnetic moment enabling magnetic dipolar coupling to radiation. Since the magnetic dipole is oriented normal to the resonator plane, the magnetic coupling is forbidden for normal incident light ($\vartheta = 0$) and goes from positive for $\vartheta > 0$ to negative for $\vartheta < 0$. In contrast, the electric dipole for both bright and dark modes is oriented along the arcs in the sample plane and the electric coupling is independent of the sign of ϑ. Qualitatively, considering a lossless high-index dielectric substrate with the angle of total internal reflection < 45° (as in the PTIR experiments), changing of the incidence angle from + 45° to - 45° changes the sign of the magnetic field relative to the electric field, thus modifying their interference from destructive to constructive. Consistently with this interpretation, the PTIR images of the same resonators obtained by rotating the prism substrate by 180° show that for parallel polarization the hot-spot intensity changes from intense to weak and vice versa (**figure S7**). In particular, the resonators illuminated for parallel polarization from the short arc side provide always the stronger hot spots.

To quantify the contributions of the dark and bright modes to the overall plasmonic response as a function of wavelength and incident angle, the conditions where either only the dark-mode or only the bright-mode are excited were identified first (see methods). Then the longer and shorter arc electrical dipole magnitudes and relative phases were identified for these two special cases. Finally, to calculate the contributions of the bright and dark modes to the resonators response from the simulation results for arbitrary optical frequencies and incident angles ϑ, a linear transformation from the basis set of longer and shorter arc dipoles to the basis set of dark and bright modes was found.

Results show (figure 5 and figure S5) that the dark-mode has a resonance peak near the free space wavelength of 971 cm^{-1} (10.3 μm) with a quality factor of approximately 3. For $\vartheta = + 45°$ excitation the magnitude of dark-mode significantly exceeds the one of bright-mode for both parallel and perpendicular polarizations because of its strong magnetic coupling (Figures 5a,b, S5a, S6). Specifically, for the perpendicular polarization (Fig 5b) the electric dipolar coupling to either the dark or the bright modes is forbidden, yet the dark mode is clearly excited (via magnetic dipolar coupling), while the bright mode is not. For the parallel polarization both modes are excited but the dark mode response is notably stronger for $\vartheta = \pm 45°$ (Fig 5a, and Fig. S5a for $\vartheta = -45°$).

Next we use parallel polarization, an excitation wavelength corresponding to the dark mode resonance (971 cm^{-1}) and study the response as a function of incidence angle. For each mode we compute the complex-valued response (e.g. amplitude and phase or real and imaginary components) by the above-mentioned projection onto the basis of bright and dark mode polarizations (Figure S6). The phase is defined relative to that of the incident electric field at the center of the resonator. We observe that the amplitude of the dark mode exceeds that of the bright mode for large tilt angles (see also insets in Figure 5c).

Figure 5c depicts the in-phase (real, black) and out-of-phase (imaginary, red) components of the dark mode response. The absolute value of the real component exceeds the absolute value of the imaginary component for the majority of the incidence angles ($\vartheta \leq -30°$; $\vartheta \geq -10°$). The real component is strongly dependent on the incidence angle and changes sign at about -20°.

As the incidence angle changes, the *z* (out-of-plane) component of the incident magnetic field vector, parallel to the magnetic dipole of the dark mode, changes sign together with the incident angle, while the incident electric field vector remains in the plane, constant and positive. For illustration, in Figure 5c the real component of the dark mode response is further broken down into the symmetric and the anti-symmetric parts with respect to the incidence angle (blue lines). The larger angularly-antisymmetric part of the response is due to the magnetic dipole, and the angularly-symmetric part to the electric dipole. The electric excitation has a 3 peak structure previously associated with electrical dipoles on dielectric substrates,[52] while we speculate that the roll-off in the magnetic excitation at larger angles is associated with the decreased interaction for angles far exceeding the total internal reflection

angle. It is interesting to note that in these structures, where the metal is surrounded by a dielectric, the electric dipolar response in the metal-only is not necessarily phase shifted 90 degrees relative to the electric field. Therefore electric and magnetic dipolar responses on resonance are not necessarily 90° out of phase with each other and are allowed to interfere.[53] Specifically, in our case the interference is constructive at positive angles and destructive at negative angles, leading to the symmetry-breaking absorption.

Discussion

It was suggested[54, 55] that plasmonic metamaterials could be used as optical constructs to manipulate local optical electric fields possibly leading to fast optical information processing in a sub-wavelength regime; practically serving the function of the basic electronic circuitry elements (resistors, capacitors, etc.) at the faster rates of optical frequencies.[56] One of the fundamental building blocks of electronic circuits is the electrical diode which enables the non-reciprocal (preferential) flow of electrons in one direction thanks to its symmetry-breaking conductance. Photonics devices rely on photons in place of electrons to carry and transfer information; however, optical non-reciprocity is harder to achieve because of the time-reversal symmetry of optical-field propagation, typically governed by linear, non-magnetic light-matter interactions. For this reason the fabrication of optical diodes is an ongoing and active field of research.[57, 58]

Plasmonic metamaterials are known to display peculiar properties, such as negative refraction[59, 60] and symmetry-breaking transmission[61, 62] which can be exploited to realize cloaking and polarization conversion devices, respectively. However, symmetry-breaking transmission or absorption by itself is not sufficient for realizing optical diodes because it does not break the time-reversal symmetry of optical mode propagation.[63] We propose here that the demonstrated strong symmetry-breaking absorption in the ASRR metamaterials near-field could be leveraged to realize optical diodes when coupling ASRRs with a *non-linear* material[64], e.g. as a coating or a substrate. Materials characterized by large Kerr nonlinearity or saturable absorbtion could be used to nonlinearly change the ASRR response, and therefore the overall reflection coefficient. Specifically, the interference of the electric and magnetic excitation channels, responsible for the symmetry-breaking absorption in ASRRs, or similar structures, will enhance the non-linear response of the material for one angle of incidence but not for the reciprocal. We speculate that for such nonlinear case the symmetry-breaking absorption will also break the optical reciprocity for the totally internally reflected light, resulting in an optical diode.

Since in ASRR the electric dipole strength is a strong function of the geometrical asymmetry, while the strength of the magnetic dipole is approximately independent of the geometrical asymmetry, the interference between the two excitation channels could be controlled and maximized by engineering their geometrical parameters.

Conclusions

In conclusion, the PTIR technique was used to observe SEIRA hot-spot intensities in the near-field of plasmonic nanostructures that are asymmetric with respect to the direction of incidence, as a function of the nanostructure orientation. Finite element calculations revealed that such symmetry-breaking absorption derives from the angle-dependent interference between electric and magnetic dipolar excitations of the dark-mode in the ASRRs. Specifically, with the convention used in this paper, such interference is constructive for positive incident angles, destructive for negative incident angles and zero for surface normal illumination ($\vartheta = 0°$).

Based on these observations, we suggest that for symmetric and slightly asymmetric SRR structures the best excitation efficiency in SEIRA experiments is obtained for illumination with linearly polarized light from the dielectric side at an angle far from surface normal for which the constructive interference of the plasmonic excitation is maximized; 35° for the structure studied here (figure 5c). Such condition could be realized using a dielectric prism, or with an ATR microscope objective, in place of the most ubiquitous Cassegrain objectives. Furthermore, we reason that the symmetry-breaking absorption revealed in this work could be exploited to realize ultra-thin, non-reciprocal reflectors and optical diodes by coating plasmonic resonators with a nonlinear material.

Experimental

Sample Fabrication

All chemicals were used as received without further purification. ASRRs arrays were fabricated directly on ZnSe prisms as follows (see figure S1). Each prism was cleaned in an ultrasonic bath with acetone (1 min) and methanol (1 min) and blown dry with a nitrogen gun. A bilayer of PMMA positive electron beam resist was spun (25 Hz) on top of the prism, using a custom adaptor piece described previously.[24] The resist then was baked in an oven (140 °C for 30 min) and an aluminum charge dissipation layer (30 nm ± 5 nm) was deposited with an electron-beam evaporator operated at a vacuum pressure of $6.67 \cdot 10^{-4}$ Pa. Electron beam lithography was used to write (dose 1350 μC/cm^2, current 200 pA) the ASRRs arrays directly on the ZnSe prisms by means of another custom adaptor piece.[24] Next, the aluminum layer was removed with a tetramethylammonium hydroxide, water solution (2.4 ml/L) and the pattern was developed in a mixture of Methyl Iso-butylketone and isopropyl alcohol. Electron beam deposition was used to deposit (0.1 nm/s at $6.67 \cdot 10^{-4}$ Pa) a thin chromium adhesion layer (≈ 5 nm) and a gold layer (150 nm ± 10 nm). Finally, the ASRRs arrays

were obtained after lift of in hot acetone (45 °C). All the fabricated arrays have dimensions of 300 μm by 300 μm with the exception of *sample-4*, which is much smaller. After preliminary characterization a 200 nm PMMA film was spun coated on the resonators arrays.

FTIR spectroscopy

Fourier Transform Infrared (FTIR) spectra were recorded at near normal incidence (fig. 2b, 2c) with an FTIR spectrometer equipped with an infrared microscope by illuminating a 200 μm by 200 μm sample area with a 36x reverse Cassegrain reflection objective (NA = 0.52) and a ZnSe wire grid polarizer (to control the light polarization). The 36x reflective objective provides illumination and collection of light with incidence angles $15° < \vartheta < 30°$ from the sample surface normal (see Fig 2b, 2c); the light between normal incidence and 15° is blocked by the objective. 128 spectra (4 cm^{-1} resolution) were acquired and averaged for each sample. The FTIR spectra were normalized with respect to the spectrum of the bare ZnSe surface (expected to have a wavelength independent reflectivity) to account for the spectral dependence of the illumination source. Because of the lower density of resonators within the focal spot sample-3 and sample-4 didn't provide sufficient signal to yield a far-field FTIR spectra with the instrumentation used in this work.

PTIR experiments

PTIR experiments were carried out using a commercial PTIR setup which consists of an AFM microscope operating in contact mode and a tunable pulsed laser source consisting of an Optical Parametric Oscillator based on a non-critically phase-matched $ZnGeP_2$ crystal. Such laser emits linearly polarized light pulses 10 ns long at 1 kHz repetition rate with wavelength tunable from 4000 cm^{-1} to ≈ 1025 cm^{-1} (from 2.5 μm to 9.76 μm). The maximum power used in the PTIR experiments was 0.2 μW. The samples on the ZnSe prisms were illuminated in total internal reflection (fig. 1a) by focusing the laser light under the AFM tip with a ZnSe lens. The typical spot size is 30 μm ± 10 μm depending on the wavelength. The low repetition rate of the laser (1 kHz) ensures that both sample and cantilever return to equilibrium between pulses. A wire grid linear polarizer was used as a variable attenuator to control the light intensity at the sample while a polarization control module, consisting of three motorized mirrors, was used to obtain the desired light polarization at the sample. All PTIR experiments were recorded with linearly, s-polarized light with the electric field vector always in the A-SRR array plane and perpendicular to the plane of incidence. An infrared pyroelectric camera was used to calibrate motorized mirror positions resulting in the laser output co-linearity in the entire wavelength range. PTIR spectra were obtained by averaging the cantilever deflection amplitude from 256 individual laser pulses at each wavelength and tuning the laser at intervals of 3 cm^{-1}. PTIR images were recorded by illuminating the sample with a constant wavelength while scanning the AFM tip. The topography and the chemical (PTIR) signals are acquired at different timescales preventing any possible crosstalk between the two channels. The AFM height and the PTIR signal acquisition was synchronized so that for each AFM pixel the PTIR signal is an average over a fixed number of laser pulses[24] (32 in this work). The pixel sizes were kept at 40 nm x 40 nm for all images. Commercially available 450 μm long silicon contact-mode AFM probes with a nominal spring constant between 0.07 N/m and 0.4 N/m were used for recording all the PTIR images and spectra.
The near field enhancement was calculated are the ratio of the spectral intensities for the PMMA CH_3 wagging mode[50] around 1190 cm^{-1}. The uncertainties in the near field enhancement represent a standard deviation in determining the peak intensity and their ratio.

Finite element Calculations

A commercial finite element solver was used for the numerical calculations. A gold resonator with external diameter of 2.0 μm, inner diameter of 0.95 μm and thickness of 150 nm was placed on a ZnSe surface, covered by a PMMA film. Cylindrical computational domain (20 μm diameter and 8 um tall) was centered on the ASRR and surrounded by 2 μm thick perfectly matched layers (PML) on all sides. The plane wave illumination was introduced at the lower boundary of the cylinder, from the ZnSe side. This boundary condition defined the incidence angle and polarization of the exciting light, while the reflected and scattered light was absorbed in the PML. In the case of parallel light polarization the simulations were carried out by illuminating the resonator for illumination angles spanning from $\vartheta = -60°$ to $\vartheta = +60°$ (figure 4a) while in the case of perpendicular polarization the calculations were obtained only for the case of $\vartheta = 45°$ (figure 4b).

To quantify the dark and bright mode response as a function of wavelength and incident angle, we first calculated the y (parallel) component of the dipole moment for each arc by integrating their y component of the electric polarization. By assuming that the total response is limited to the superposition of the bright and dark modes, we can use a simple linear transformation to go from the basis of longer and shorter arc dipoles to the basis of dark and bright modes. To make such transformation, we found the linear combinations of longer (shorter) arc dipoles corresponding to each of the two modes, by using incidence conditions where either only the dark mode or only the bright mode is excited. Arc dipole moments under perpendicular excitation at 971 cm^{-1} (10.3 μm) vacuum wavelength were used to define the dark-mode basis vector, as the bright mode response is negligible in this case. Bright mode vector was set using surface-normal excitation at 15 μm - dark mode magnetic coupling at this angle is negligible and the excitation frequency is far away from its resonance peak. We verified this basis set by checking that the calculated dark mode resonance peak shape and center wavelength were independent of the incidence angle and direction.

Acknowledgements

B. L. acknowledges support under the Cooperative Research Agreement between the University of Maryland and the National Institute of Standards and Technology Center for Nanoscale Science and Technology, Award 70NANB10H193, through the University of Maryland.

Notes and references

Electronic Supplementary Information (ESI) available: nanofabrication scheme, Schematic description of ASRR arrays, supplementary discussion. See DOI: 10.1039/b000000x/

1 Citations here in the format A. Name, B. Name and C. Name, *Journal Title*, 2000, **35**, 3523; A. Name, B. Name and C. Name, *Journal Title*, 2000, **35**, 3523.

1. L. R. Hirsch, R. J. Stafford, J. A. Bankson, S. R. Sershen, B. Rivera, R. E. Price, J. D. Hazle, N. J. Halas and J. L. West, *Proc. Natl. Acad. Sci. U. S. A.*, 2003, **100**, 13549-13554.
2. J. H. Park, G. von Maltzahn, L. L. Ong, A. Centrone, T. A. Hatton, E. Ruoslahti, S. N. Bhatia and M. J. Sailor, *Adv. Mater.*, 2010, **22**, 880-885.
3. H. A. Atwater and A. Polman, *Nat. Mater.*, 2010, **9**, 205-213.
4. F. Neubrech, A. Pucci, T. W. Cornelius, S. Karim, A. Garcia-Etxarri and J. Aizpurua, *Phys. Rev. Lett.*, 2008, **101**, 157403.
5. K. Kneipp, H. Kneipp, I. Itzkan, R. R. Dasari and M. S. Feld, *Chem. Rev.*, 1999, **99**, 2957-2975.
6. W. E. Doering and S. M. Nie, *J. Phys. Chem. B*, 2002, **106**, 311-317.
7. A. D. McFarland, M. A. Young, J. A. Dieringer and R. P. Van Duyne, *J. Phys. Chem. B*, 2005, **109**, 11279-11285.
8. G. von Maltzahn, A. Centrone, J. H. Park, R. Ramanathan, M. J. Sailor, T. A. Hatton and S. N. Bhatia, *Adv. Mater.*, 2009, **21**, 3175-3180.
9. F. Le, D. W. Brandl, Y. A. Urzhumov, H. Wang, J. Kundu, N. J. Halas, J. Aizpurua and P. Nordlander, *ACS Nano*, 2008, **2**, 707-718.
10. B. Lahiri, G. Holland, V. Aksyuk and A. Centrone, *Nano Lett.*, 2013, **13**, 3218-3224.
11. R. Adato, A. A. Yanik, J. J. Amsden, D. L. Kaplan, F. G. Omenetto, M. K. Hong, S. Erramilli and H. Altug, *Proc. Natl. Acad. Sci. U. S. A.*, 2009, **106**, 19227-19232.
12. C. H. Wu, A. B. Khanikaev, R. Adato, N. Arju, A. A. Yanik, H. Altug and G. Shvets, *Nat. Mater.*, 2012, **11**, 69-75.
13. K. Chen, R. Adato and H. Altug, *ACS Nano*, 2012, **6**, 7998-8006.
14. H. Aouani, H. Sipova, M. Rahmani, M. Navarro-Cia, K. Hegnerova, J. Homola, M. H. Hong and S. A. Maier, *ACS Nano*, 2013, **7**, 669-675.
15. V. A. Fedotov, M. Rose, S. L. Prosvirnin, N. Papasimakis and N. I. Zheludev, *Phys. Rev. Lett.*, 2007, **99**, 147401.
16. C. Debus and P. H. Bolivar, *Appl. Phys. Lett.*, 2007, **91**, 184102.
17. B. Luk'yanchuk, N. I. Zheludev, S. A. Maier, N. J. Halas, P. Nordlander, H. Giessen and C. T. Chong, *Nat. Mater.*, 2010, **9**, 707-715.
18. B. Lahiri, A. Z. Khokhar, R. M. De La Rue, S. G. McMeekin and N. P. Johnson, *Opt. Express*, 2009, **17**, 1107-1115.
19. P. Alonso-Gonzalez, P. Albella, F. Golmar, L. Arzubiaga, F. Casanova, L. E. Hueso, J. Aizpurua and R. Hillenbrand, *Opt. Express*, 2013, **21**, 1270-1280.
20. M. W. Knight, J. Fan, F. Capasso and N. J. Halas, *Opt. Express*, 2010, **18**, 2579-2587.
21. J. H. Shi, E. Plum, V. A. Fedotov, N. I. Zheludev and A. Electromagnetics, in *Piers 2011 Suzhou: Progress in Electromagnetics Research Symposium*, 2011, pp. 567-571.
22. C. Enkrich, M. Wegener, S. Linden, S. Burger, L. Zschiedrich, F. Schmidt, J. F. Zhou, T. Koschny and C. M. Soukoulis, *Phys. Rev. Lett.*, 2005, **95**.
23. A. Dazzi, R. Prazeres, E. Glotin and J. M. Ortega, *Opt. Lett.*, 2005, **30**, 2388-2390.
24. B. Lahiri, G. Holland and A. Centrone, *Small*, 2013, **9**, 439-445.
25. A. M. Katzenmeyer, V. Aksyuk and A. Centrone, *Anal. Chem.*, 2013, **85**, 1972-1979.
26. C. Marcott, M. Lo, K. Kjoller, C. Prater and I. Noda, *Appl. Spectrosc.*, 2011, **65**, 1145-1150.
27. A. Dazzi, R. Prazeres, F. Glotin, J. M. Ortega, M. Al-Sawaftah and M. de Frutos, *Ultramicroscopy*, 2008, **108**, 635-641.
28. J. R. Felts, K. Kjoller, M. Lo, C. B. Prater and W. P. King, *ACS Nano*, 2012, **6**, 8015-8021.
29. A. J. Harrison, E. A. Bilgili, S. P. Beaudoin and L. S. Tayor, *Anal. Chem.*, 2013, **85**, 11449-11455.
30. E. Kennedy, R. Al-Majmaie, M. Al-Rubeai, D. Zerulla and J. H. Rice, *J Biophotonics*, 2013, DOI: 10.1002/jbio.201300138.
31. A. Dazzi, R. Prazeres, F. Glotin and J. M. Ortega, *Ultramicroscopy*, 2007, **107**, 1194-1200.
32. K. Aydin, I. M. Pryce and H. A. Atwater, *Opt. Express*, 2010, **18**, 13407-13417.
33. S. Lal, N. K. Grady, J. Kundu, C. S. Levin, J. B. Lassiter and N. J. Halas, *Chem. Soc. Rev.*, 2008, **37**, 898-911.
34. B. Lahiri, S. G. McMeekin, R. M. De La Rue and N. P. Johnson, *Applied Physics Letters*, 2011, **98**, 153116.
35. R. Vogelgesang and A. Dmitriev, *Analyst*, 2010, **135**, 1175-1181.
36. P. Alonso-Gonzalez, M. Schnell, P. Sarriugarte, H. Sobhani, C. H. Wu, N. Arju, A. Khanikaev, F. Golmar, P. Albella, L. Arzubiaga, F. Casanova, L. E. Hueso, P. Nordlander, G. Shvets and R. Hillenbrand, *Nano Lett.*, 2011, **11**, 3922-3926.
37. T. Zentgraf, J. Dorfmuller, C. Rockstuhl, C. Etrich, R. Vogelgesang, K. Kern, T. Pertsch, F. Lederer and H. Giessen, *Opt. Lett.*, 2008, **33**, 848-850.
38. E. Yoxall, M. Navarro-Cia, M. Rahmani, S. A. Maier and C. C. Phillips, *Appl. Phys. Lett.*, 2013, **103**, 213110.

39. R. L. Olmon, P. M. Krenz, A. C. Jones, G. D. Boreman and M. B. Raschke, *Opt. Express*, 2008, **16**, 20295-20305.
40. S. E. Grefe, D. Leiva, S. Mastel, S. D. Dhuey, S. Cabrini, P. J. Schuck and Y. Abate, *Phys. Chem. Chem. Phys.*, 2013, **15**, 18944-18950.
41. B. Knoll and F. Keilmann, *Opt. Commun.*, 2000, **182**, 321-328.
42. A. Cvitkovic, N. Ocelic and R. Hillenbrand, *Opt. Express*, 2007, **15**, 8550-8565.
43. M. Brehm, T. Taubner, R. Hillenbrand and F. Keilmann, *Nano Lett.*, 2006, **6**, 1307-1310.
44. I. M. Craig, M. S. Taubman, A. S. Lea, M. C. Phillips, E. E. Josberger and M. B. Raschke, *Opt. Express*, 2013, **21**, 30401-30414.
45. A. Dazzi, C. B. Prater, Q. C. Hu, D. B. Chase, J. F. Rabolt and C. Marcott, *Appl. Spectrosc.*, 2012, **66**, 1365-1384.
46. J. R. Felts, S. Law, C. M. Roberts, V. Podolskiy, D. M. Wasserman and W. P. King, *Appl. Phys. Lett.*, 2013, **102**, 152110.
47. A. M. Katzenmeyer, J. Canivet, G. Holland, D. Farrusseng and A. Centrone, *Angew. Chem. Int. Ed.*, 2014, **53**, 2852-2856.
48. C. Mayet, A. Dazzi, R. Prazeres, E. Allot, E. Glotin and J. M. Ortega, *Opt. Lett.*, 2008, **33**, 1611-1613.
49. A. M. Katzenmeyer, J. Chae, R. Kasica, G. Holland, B. Lahiri and A. Centrone, *Adv. Optical Mater.*, 2014, **2**, 718-722.
50. D. Lin-Vien, N. B. Colthup, W. G. Fately and J. G. Grasselli, eds., *handbook of infrared and raman characteristic frequencies of organic molecules*, Academic Press, Boston, 1991.
51. E. D. Palik, *Handbook of Optical Constants of Solids*, Academic Press, San Diego, 1998.
52. K. B. Crozier, Z. Wenqi, W. Dongxing, L. Shiyun, M. D. Best and J. P. Camden, *Selected Topics in Quantum Electronics, IEEE Journal of*, 2014, **20**, 152-162.
53. I. Sersic, C. Tuambilangana, T. Kampfrath and A. F. Koenderink, *Phys. Rev. B*, 2011, **83**.
54. N. Engheta, *Science*, 2007, **317**, 1698-1702.
55. A. Alu and N. Engheta, *Phys. Rev. Lett.*, 2009, **103**.
56. V. J. Sorger, R. F. Oulton, R. M. Ma and X. Zhang, *Mrs Bulletin*, 2012, **37**, 728-738.
57. L. Feng, M. Ayache, J. Q. Huang, Y. L. Xu, M. H. Lu, Y. F. Chen, Y. Fainman and A. Scherer, *Science*, 2011, **333**, 729-733.
58. L. Fan, J. Wang, L. T. Varghese, H. Shen, B. Niu, Y. Xuan, A. M. Weiner and M. H. Qi, *Science*, 2012, **335**, 447-450.
59. J. B. Pendry, *Phys. Rev. Lett.*, 2000, **85**, 3966-3969.
60. R. A. Shelby, D. R. Smith and S. Schultz, *Science*, 2001, **292**, 77-79.
61. V. A. Fedotov, A. S. Schwanecke, N. I. Zheludev, V. V. Khardikov and S. L. Prosvirnin, *Nano Lett.*, 2007, **7**, 1996-1999.
62. C. Menzel, C. Helgert, C. Rockstuhl, E. B. Kley, A. Tunnermann, T. Pertsch and F. Lederer, *Phys. Rev. Lett.*, 2010, **104**.
63. D. Jalas, A. Petrov, M. Eich, W. Freude, S. H. Fan, Z. F. Yu, R. Baets, M. Popovic, A. Melloni, J. D. Joannopoulos, M. Vanwolleghem, C. R. Doerr and H. Renner, *Nat. Photonics*, 2013, **7**, 579-582.
64. M. F. Yanik, S. H. Fan, M. Soljacic and J. D. Joannopoulos, *Opt. Lett.*, 2003, **28**, 2506-2508.

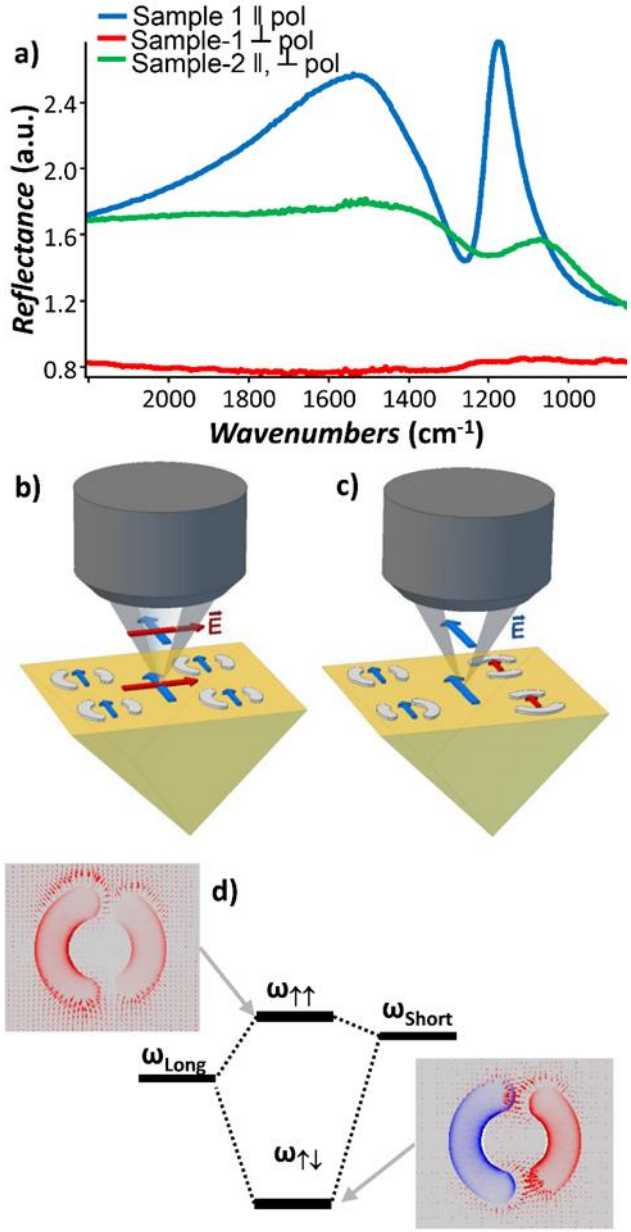

Figure 1. a) FTIR spectra of ASRRs arrays. The schematic of the FTIR experiments for sample-1 (b) and sample-2 (c). The IR Cassegrain objective illuminates and collects light with incidence angles $15° < \vartheta < 30°$ with respect to the sample surface normal; the light with $0° < \vartheta < 15°$ is blocked by the objective. For sample-1 (b) the light polarization used in the experiments is either parallel (blue arrows) or perpendicular (red arrows) to all resonators. For sample-2 (c) because of the different orientation of the resonators the light polarization is parallel for half of the resonators (blue arrows) and perpendicular to the other half (red arrows). The FTIR spectra are displayed in common intensity scale and normalized with respect to a bare ZnSe background. (d) The fundamental resonances of the short and long arcs hybridize to form symmetric (bright) and antisymetric (dark) modes, The red arrows denote electric field vectors; the color denotes the component of polarization vector in the direction of the arcs, vertical in the image (color code, red is positive, blue negative).

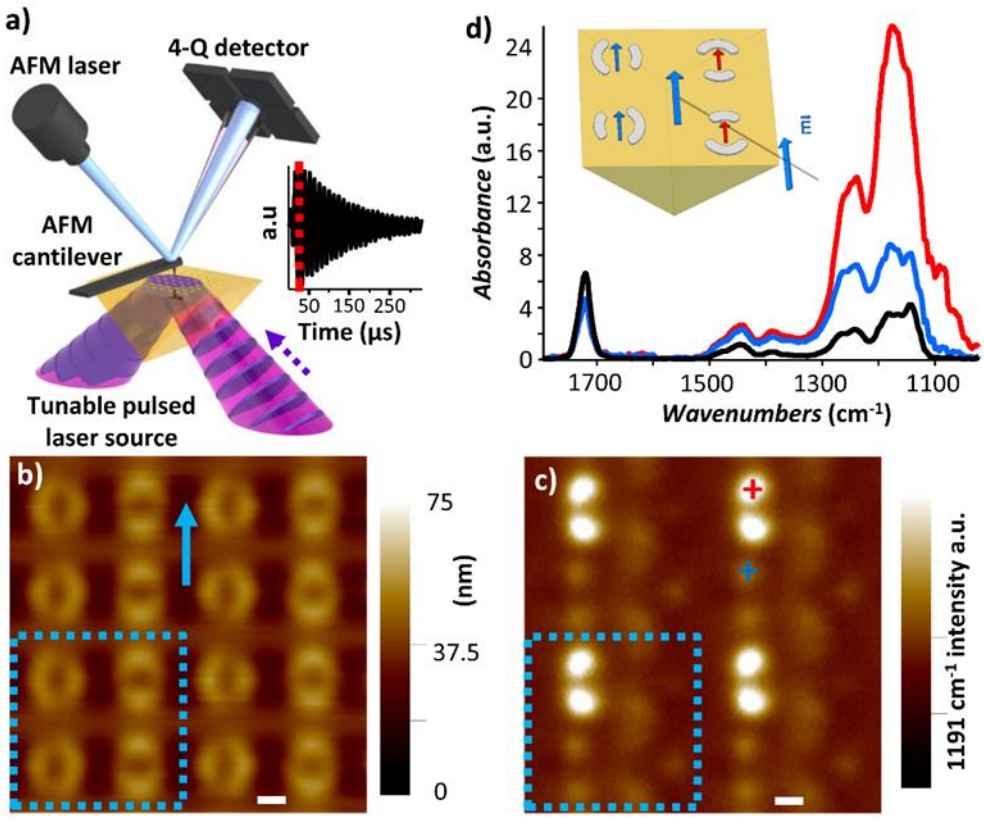

Figure 2. a) Schematic of the PTIR measurement. The laser beam (pink) illuminates the sample by total internal reflection to minimize the direct light-tip interaction. When the IR laser pulses (purple) are absorbed by the sample this thermally expands deflecting the AFM cantilever. The deflection amplitude signal (inset) is proportional to the absorbed energy and it is measured by the AFM four-quadrant detector on a time scale much faster than the AFM feedback. The red dotted bar in the inset represent the maximum of the peak to peak deflection used to measure the local IR spectra and maps. b) AFM height image of sample-2 coated with a 200 nm PMMA film. The dotted squares identify a single unit cell in the array; scale bars are 500 nm and the blue arrow indicates the direction of the electric field polarization in the PTIR experiments. c) PTIR image of the PMMA CH3 wagging mode at 1191 cm^{-1} (8.40 µm) showing near-field SEIRA hot spots in the PMMA layer d) PTIR spectra for PMMA recorded 300 µm away from the ASRRs (black, used as reference) and on the hot spots marked as "+" in panel c (red and blue), respectively. The PTIR spectra are displayed in common intensity scale. The inset depicts a unit cell of the sample-2 array and illumination schematic: the resonators are excited by light impinging at 45° from the right hand side with the electric field polarization in the sample plane, parallel for two resonators in each unit cell (blue arrows) and perpendicular for the other two (red arrows). For the two resonators illuminated with parallel polarization the incidence angle is $\vartheta = \pm$ 45° relative to the resonators orientation.

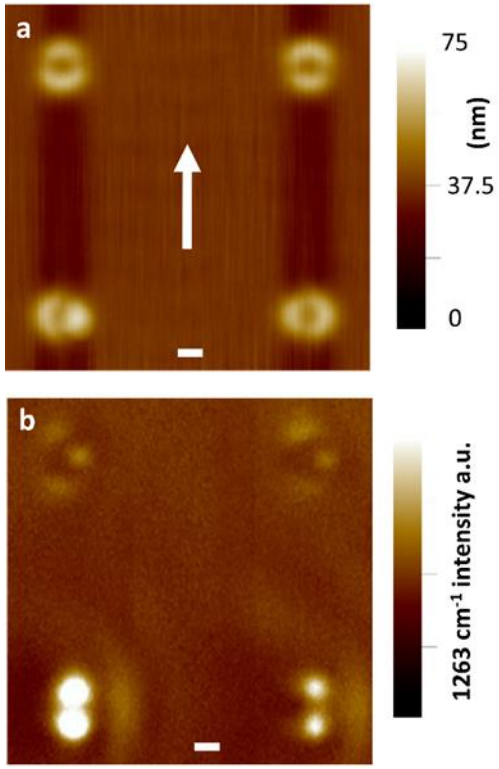

Figure 3. a) AFM height image of sample-3 coated with a 200 nm PMMA film; the white arrow indicates the direction of the electric field polarization in the PTIR experiments. b) Corresponding PTIR image of the PMMA C-O stretching vibrational mode at 1263 cm^{-1} (7.92 µm). The PTIR image shows differences in the near-field hot spots intensity as a function of the resonators orientation and show that, the light is preferentially scattered by the resonators in the right direction. Scale bars are 1.0 µm.

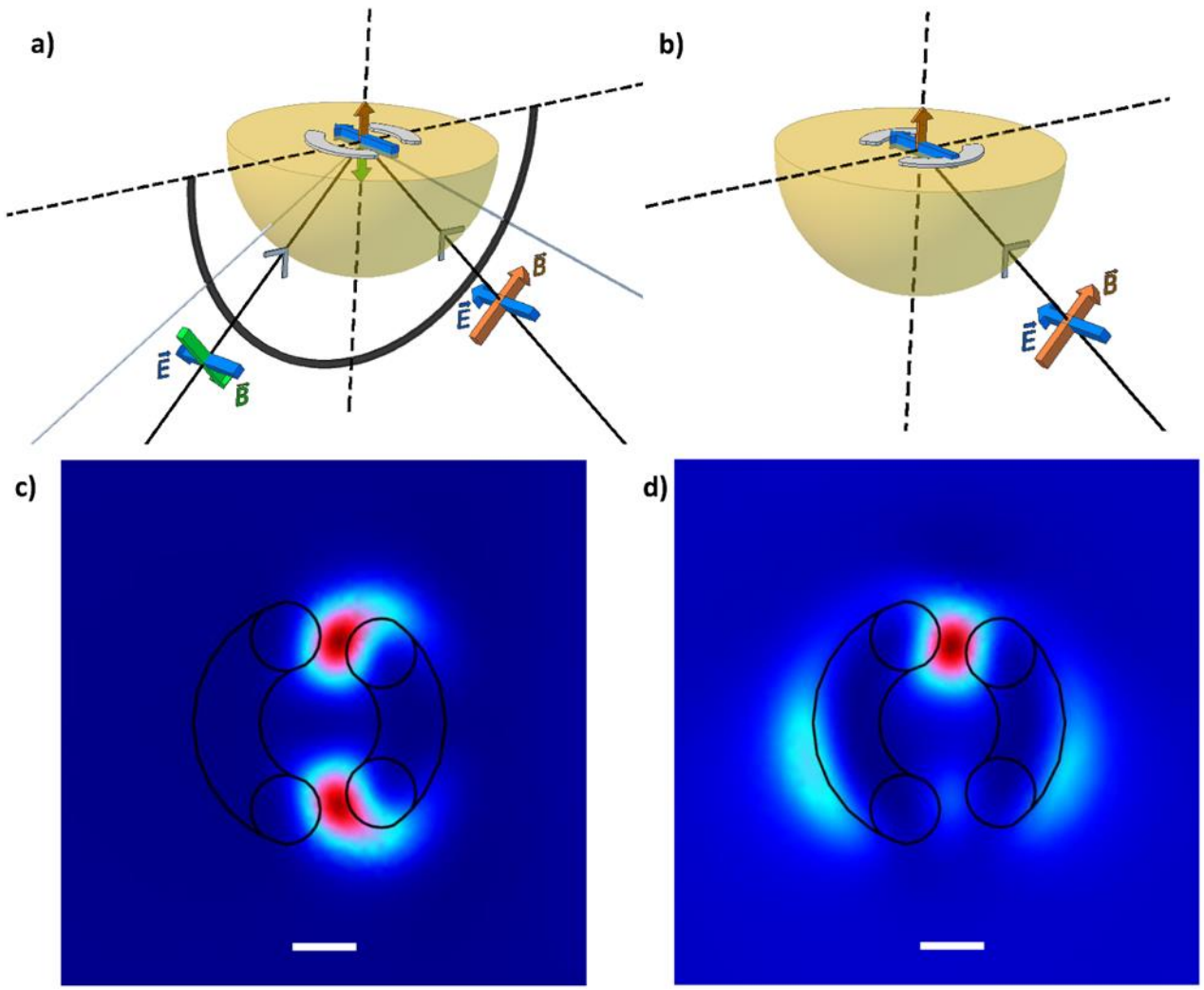

Figure 4. Schematic illustrating the illumination angles used in the numerical modeling of PTIR experiments in case of parallel polarization (a) or perpendicular polarization (b).The blue arrows show the electric field vector; the orange and green arrows show the magnetic vector. All line and arrows in panels a,b are in the plane defined by the black dotted lines with the exception of the electric field arrows which are perpendicular to that plane. Results obtained when illuminating the structure with s-polarized 1191 cm^{-1} (8.4 µm) light at c) + 45° with parallel polarization and d) 45° with perpendicular polarization. The figure shows the energy density in PMMA integrated along the film thickness (z) and convolved with a 200 nm waste Gaussian peak function (similar to the film thickness) to approximately account for the thermal and mechanical effects of the PTIR experiment. Scale bars are 500 nm.

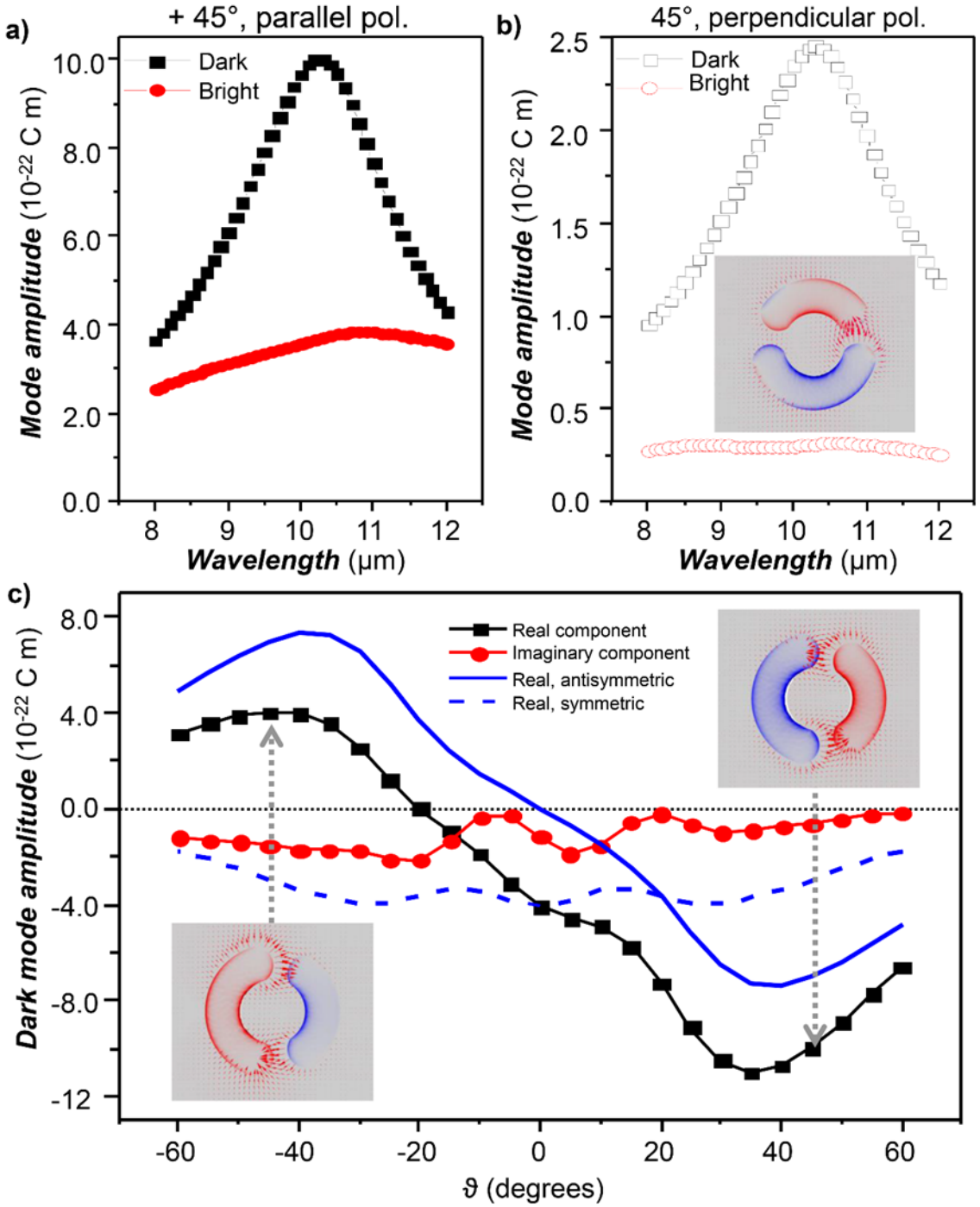

Figure 5. Numerical modeling of ASRR polarization as a function of wavelength (a,b) and the incidence angle ϑ (c). The dark-mode resonance 971 cm^{-1} (10.3 μm) is excited by s-polarized light incident at 45° for both parallel and perpendicular polarizations, while the bright mode is broad and it is weakly excited, only by the parallel polarization. The real and imaginary components of the dark-mode are shown in panel c. The response of the dark-mode is predominantly in-phase with incident electric field (real component) and antisymmetric with respect to the incidence angle, both characteristic of magnetic excitation. The absolute value of the response is different for +45° and -45° incidence angle because of the constructive (destructive) interference of the electric and magnetic excitation. The insets are for slice plane half way through the ASRR thickness and show the electric field (arrows) and the component of polarization vector in the direction of the arcs, vertical in the image (color code, red is positive).

Table of content graphic:

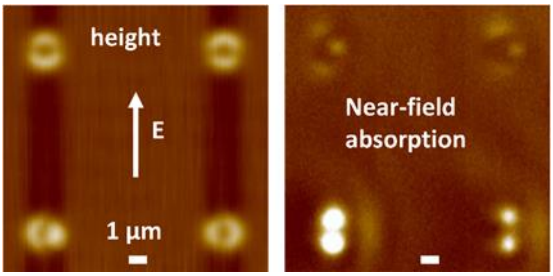

PTIR reveal symmetry-breaking near-field SEIRA enhancements caused by the interference between electric and magnetic excitations of the resonators' dark-mode.